Magnetic properties of nanocrystalline $La_{1-x}MnO_{3+\delta}$ manganites: size effects

Magnetic properties of nanocrystalline $La_{1-x}MnO_{3+\delta}$ manganites: size effects

V Markovich[1,6], I Fita[2,3], D Mogilyansky[4,5], A Wisniewski[2], R Puzniak[2], L Titelman[4], L Vradman[4], M Herskowitz[5] and G Gorodetsky[1]

[1] Department of Physics, Ben-Gurion University of the Negev, PO Box 653, 84105 Beer-Sheva, Israel
[2] Institute of Physics, Polish Academy of Sciences, Aleja Lotnikow 32/46, 02-668 Warsaw, Poland
[3] Donetsk Institute for Physics and Technology, National Academy of Sciences, 83114 Donetsk, Ukraine
[4] Department of Chemical Engineering, Sami Shamoon College of Engineering, 84100 Beer-Sheva, Israel
[5] Blechner Center for Industrial Catalysis and Process Development, Department of Chemical Engineering, Ben-Gurion University of the Negev, 84105 Beer-Sheva, Israel

E-mail: markoviv@bgu.ac.il

Abstract

The magnetic properties of nanocrystalline manganites $La_{1-x}MnO_{3+\delta}$ with particle size of 20 (LMO20), 25 (LMO25), and 30 nm (LMO30), prepared by the citrate method, have been investigated in the temperature range 5–320 K, magnetic field up to 90 kOe and under quasi-hydrostatic pressures up to 14.5 kbar. The studies involve sequential zero-field-cooled magnetization (M) measurements followed by magnetization measurements during cooling in the same magnetic field (H) and complementary measurements of ac susceptibility. Additional measurements of M versus H were carried out at ambient and applied pressures. All nanoparticles exhibit a paramagnetic to ferromagnetic transition (PFT) at a Curie temperature $T_C > 200$ K. It was found that the relative volume of the ferromagnetic phase increases for larger particle size and approaches a value of about 93% for LMO30. The real part of the ac susceptibility of sample LMO20 exhibits strong frequency dependence in a wide temperature range below T_C, whereas for sample LMO30 only relatively weak frequency dependence was observed. The magnetization of sample LMO30 exhibits a PFT of second order; the type of transition could not be established for the smaller particles. It was found that an applied pressure enhances the T_C of $La_{1-x}MnO_{3+\delta}$ nanoparticles with a pressure coefficient of $dT_C/dP \approx 1.9$ K kbar^{-1} for LMO20 and $dT_C/dP \approx 1.4$ K kbar^{-1} for LMO25 and LMO30 samples. Peculiar magnetic memory effects observed for sample LMO20 are discussed.

(Some figures in this article are in colour only in the electronic version)

---

[6] Author to whom any correspondence should be addressed.

1. Introduction

Doped rare-earth perovskite manganites $(R_{1-x}A_x)MnO_3$ (R is a rare-earth ion and A is a divalent ion such as Ca, Sr, Ba, etc), well known for their colossal magnetoresistance (CMR) properties, have been studied extensively in the last decade [1, 2]. In general, these systems comprise a strong competition between charge, orbital, lattice, and magnetic degrees of freedom, all of which make them an intriguing subject of research. Recently, renewed interest was triggered by their possible applications in magnetoresistive devices. Since the magnetoresistance of manganites is most prominent near the paramagnetic to ferromagnetic transition (PFT) temperature, the relatively low Curie temperatures, T_C, of most CMR oxides are the main hindrance to their practical applications. Thus, it is desirable to have manganites with T_C preferably close to room temperature. A significant potential of manganites is the possibility of inducing ferromagnetism by cationic substitutions at different sites in the antiferromagnetic (AFM) parent compound $LaMnO_3$ (LMO) showing a Néel temperature of $T_N \approx 140$ K [1, 2]. A variety of magnetic and crystallographic structures have been observed in the parent compound $LaMnO_3$, due to off-stoichiometry on the lanthanum as well as on the manganese sites: AFM, canted, spin glass, ferromagnetic (FM) insulator, or even FM metal with high enough T_C [3, 4].

Magnetic nanoparticles are currently the focus of intense investigations due to the physics they involve and their potential technological applications, such as in logic circuits, magneto-electronic devices, magnetic data storage, biomedicine. When the size of the magnetic nanoparticles is reduced to few nanometres, some of their basic magnetic properties, e.g., the spontaneous magnetization, the Curie temperature, and the coercivity, are strongly influenced by the particle size and may differ significantly from the bulk properties. As the particle size decreases, the surface and interface effects become more and more important. The presence of defects, broken bonds, fluctuations in number of atomic neighbours and interatomic distances, results in topological and magnetic disorder at the surface and may cause a decrease in the magnetization value. For various manganite nanoparticles of few tens of nanometres size, a core–shell structure was proposed [5–8]. In this model the inner part of the particle, i.e., the core, has the same properties as the bulk material, whereas the outer layer, namely, a shell with width t, contains most of the oxygen faults and vacancies in the crystallographic structure, leading to a magnetically dead layer. It is quite well established that the relative shell thickness t increases with the decrease in grain size [6–8].

This study was motivated by recent investigations [9, 10] of $La_{1-x}MnO_{3+\delta}$ nanocrystalline compounds which exhibit $T_C > 200$ K. It is worth noting that Dezanneau *et al* [9] performed their studies on samples of various crystalline sizes with different La/Mn ratio in the precursor solution. It was found that the temperature of the onset of ferromagnetism and the sharpness of the PFT increase as the average La/Mn ratio decreases down to La/Mn ~ 0.9. For samples with $0.8 \leqslant$ La/Mn $\leqslant 0.9$, the temperature of the magnetic transition $T_C(\text{onset}) \sim 250$ K is almost unchanged, but the PFT remains very broad and occurs in an about 100 K wide temperature range [9]. Controversial observations for $LaMnO_3$ nanoparticles have shown that the field-cooled (FC) magnetization increases by 100 times with decreasing particle size from 54 to 19 nm, whereas the temperature at which there is a sharp rise of the magnetization (possibly T_C) varies only slightly [10]. This study contrasts strongly with many other observations obtained for ferromagnetic Ca-doped [7, 11] and Sr-doped [12–14] $LaMnO_3$ nanoparticles exhibiting a magnetization increase with increasing particle size.

Recently, Sun *et al* [15] have observed a striking magnetization memory effects in interacting $Ni_{81}Fe_{19}$ nanoparticles (6 nm). Similar observations were also performed by Tsoi *et al* [16] on other nanoparticle systems (γ-Fe_2O_3–alginate nanocomposite with average

particle size of $\sim$4 nm) and on Co nanoparticles [17] with an average diameter of 5 nm. It should be emphasized that the origin of salient memory effects in magnetic nanoparticles is still largely debated [15–20].

Hydrostatic pressure (P) is yet an additional parameter that may tune the structural characteristics of manganites. The first works [21, 22] on the pressure effect on mixed valent manganites revealed an enhancement of Curie temperature with increasing pressure. This was related to the pressure-induced compression of the lattice and to the corresponding increase of the Mn–O–Mn bond angle, resulting in a more cubic unit cell, and thereby leading to a weakening of electron–lattice coupling [22–24]. As a result, the overlapping of the e_g (Mn^{3+}) orbitals and the 2p (O^{2-}) orbital increases and the electron hopping rate is enhanced, which favours a charge delocalization and ferromagnetic double exchange (DE) interactions. Thus, studies of the magnetization and magnetic transition temperature under an applied pressure are valuable in order to get more insight into the nature of magnetic interactions. To the best of our knowledge, no data regarding the pressure effect on the magnetic properties of manganite nanoparticles have been published.

In this work we report on measurements of the magnetization and ac susceptibility of nanocrystalline $La_{1-x}MnO_{3+\delta}$ particles with average size of 20, 25, 30 nm. The main objective is to understand the variation of magnetic properties as a function of the particle size. The nature of the magnetic phase transitions and the effect of applied quasi-hydrostatic pressure on the magnetic transition temperature are also discussed.

2. Experiment

The nanocrystalline $La_{1-x}MnO_{3+\delta}$ particles were prepared by the well-known citrate method [25]. Lanthanum nitrate hexahydrate, $La(NO_3)_3 \cdot 6H_2O$ 99.9% (Aldrich), manganese nitrate hexahydrate $Mn(NO_3)_2 \cdot 6H_2O$ 98% (Aldrich) and citric acid $HOC(CO_2H)(CH_2CO_2H)_2$ 99% (Aldrich) without further purification were taken in proportion to obtain a cation La/Mn ratio equal to 0.8. The molar amount of citric acid was equal to the sum of La and Mn cations. Lanthanum and manganese nitrates were dissolved in 0.05 mol aqueous solution of citric acid. The ratio of La/Mn was chosen to reach the maximal $T_C = 252$ K, as was found for self-doped $La_{1-x}MnO_{3+\delta}$ particles (see [9]). The solution was continuously stirred at room temperature for 24 h and evaporated from open glass under stirring at 70 °C for 4 h until a gel was formed. Evaporation was prolonged in vacuum at room temperature for 4 h and at 70 °C overnight. Then the powder in the low layer was dried at 100 °C for 24 h, heated at a rate of 1 °C min^{-1} to the desired temperature (700, 800 and 900 °C) and calcined at these temperatures for 8 h to get a series of $La_{1-x}MnO_{3+\delta}$ nanocrystalline powder having varying grain sizes.

The La and Mn contents were estimated by energy-dispersive x-ray spectroscopy (EDX) analysis with a JEOL JEM 5600 scanning electron microscope (SEM) as the average of ten measurements at different points of the sample. The x-ray powder diffraction patterns were collected on a Huber Imaging Plate Guinier camera G670 installed on an Ultrax-18 Rigaku x-ray rotating Cu anode source, with a focused monochromator (focal length $B = 360$ mm) on the incident beam providing pure Kα_1 radiation. The data were collected for 60 min at 40 kV and 90 mA. The 2θ range of the imaging plate was 0°–100°. Transmission electron microscopy was carried out on a JEOL FasTEM-2010 transmission electron microscope (TEM) operated at 200 kV. N$_2$-adsorption experiments were carried out at the temperature of liquid nitrogen with a NOVA-2000 (Quantachrome, version 7.02) instrument. The samples were outgassed under vacuum at 523 K. The specific surface areas were estimated using conventional Brunauer–Emett–Teller (BET) method [26].

Cylinder-shaped samples, having a diameter of 1 mm and height of 4.0 mm, were used for measurements of magnetization under hydrostatic pressure. The samples were prepared by

compaction of nanoparticle powder under pressure applied at room temperature. Magnetization measurements on nanoparticles compacted at different applied pressures ranging from 2 to 15 kbar showed no significant differences in their magnetic properties. Because of this, for simplicity and for better comparison, all cylinder-shaped samples were prepared at the same compaction of nanoparticle powder under a pressure of 2 kbar.

The measurements of magnetization were performed in the temperature range 5–300 K and magnetic fields up to 16 kOe, using a PAR (Model 4500) vibrating sample magnetometer. A miniature container of CuBe with an inside diameter of 1.4 mm was used as a pressure cell [27]. The pressure at low temperatures was determined by the known pressure dependence of the superconducting transition temperature of pure tin, placed near the investigated sample. As a pressure-transmitting medium we utilized a mixture of mineral oil and kerosene. The reduction of pressure during cooling to 5 K in a clamped low-temperature piston–cylinder pressure cell was taken into account in the evaluation of the pressure dependence of the Curie temperature [28]. Hereafter, for the results of measurements under an applied pressure, we shall consider for the temperature dependences of magnetization the value of pressure at room temperature, while for M versus H dependences at $T = 5$ K we shall refer to the value of pressure at low temperatures.

The measurements of the temperature dependences of the magnetization in the range 5 K $< T <$ 300 K were performed according to the following procedure: the samples were cooled in zero magnetic field to $T = 5$ K and the magnetization was measured upon heating (ZFC curve) and immediately thereafter upon cooling (FC curve) in constant magnetic field. The field dependences $M(H)$ were recorded at $T = 5$ K after zero-field cooling. The measurements of ac susceptibility at various frequencies and measurements of magnetization in high magnetic field were performed using the ACMS option of a Quantum Design physical property measurement system.

3. Results

3.1. X-ray diffraction

The powders prepared by the technique described above were analysed by x-ray powder diffraction (XRD), transmission electron microscope (TEM) and N_2-adsorption methods. The XRD pattern of as-prepared sample (before heating) exhibits fully amorphous phase. During calcinations the crystallization and grain growth of the perovskite manganite phase take place. The amount of retained amorphous phase (AP) is still noticeable in the sample annealed at 700 °C, and strongly decreases after higher-temperature (800 and 900 °C) annealing. Simultaneously, manganese oxide Mn_3O_4 as a parasitic phase appears in the sample annealed at 800 °C, and its amount increases with increasing temperature of the annealing; see figure 1(a). The appearance of a parasitic Mn_3O_4 phase and its contribution to the magnetic properties of self-doped $La_{1-x}MnO_{3+\delta}$ nanoparticles was recently discussed in great detail by Dezanneau *et al* [9].

The crystal structure of manganite nanoparticles was identified to be in the rhombohedral system of $R\bar{3}C$ space group (no. 167) using hexagonal axes. The average crystallite size of the rhombohedral manganites was calculated using the Debye–Scherrer equation $\langle D \rangle = 0.9\lambda/b\cos\theta$, for the (024) reflection, where $\lambda = 1.54059$ Å for the Cu Kα_1 line, b is the full width at half maximum of the x-ray diffraction peak, and θ is the corresponding Bragg angle. It was found that $\langle D \rangle = 20$, 25, and 30 nm for samples annealed at 700, 800 and 900 °C, respectively. These samples will be denoted hereinafter as LMO20, LMO25 and LMO30, respectively. The error in the determination of the average particle size did not exceed ± 1 nm.
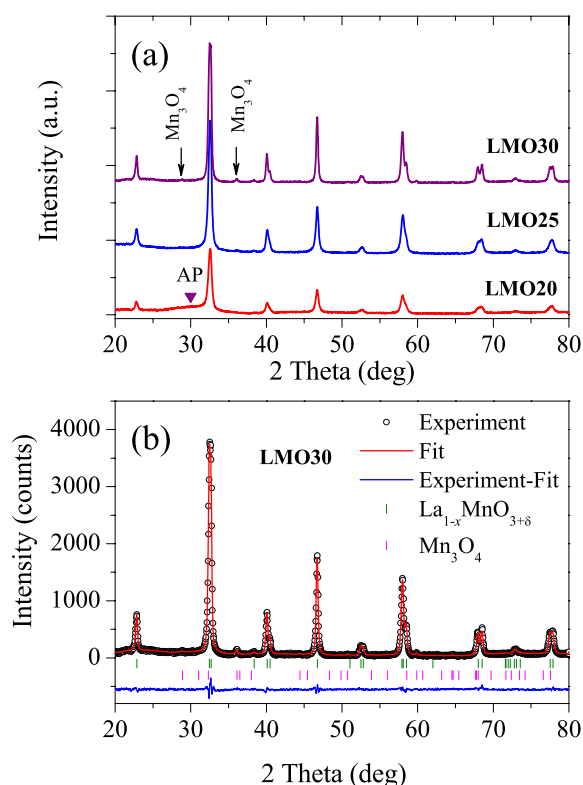
Figure 1. (a) XRD spectra of samples LMO20, LMO25 and LMO30, annealed at 700, 800, and 900 °C, respectively. The main peaks are referred to rhombohedral manganite. The most intensive reflections of manganese oxide Mn_3O_4 are indicated by arrows and the halo from the amorphous phase (AP) is shown by a triangle (▼); (b) Rietveld plot for LMO30 sample. The observed data points are indicated by open circles, and the calculated and difference patterns are shown by solid lines. The Bragg positions of the reflections of manganite and Mn_3O_4 are indicated by vertical lines below the pattern.

Specific surface areas of 43, 32 and 16 m^2 g^{-1} were measured for LMO20, LMO25 and LMO30 samples, respectively, in good correlation with the average crystallite size. The powder particle morphology for sample LMO20 shows (see figure 2(a)) that the powders consist of irregularly shaped small particles. A high-resolution TEM image (figure 2(b)) indicates that these particles are composed of many nanometric crystallites.

The Rietveld method using the FullProf-2K package [29] was employed in order to refine the crystal structure. The profile of the diffraction line was fitted using a pseudo-Voigt function and the background was modelled for 13–15 measured background points and linearly interpolated for intermediate values. The atomic site positions compatible with $R\bar{3}C$ space group are La(0, 0, 0.25) in 6a, Mn(0, 0, 0) in 6b and O(x, 0, 0.25) in 18e, where $x \approx 0.46$. All atomic sites were considered as fully occupied and only the La site occupancy was refined. The final Rietveld's refinement shows that the La/Mn ratios for LMO20, LMO25, and LMO30 samples (0.88, 0.93, and 0.96, respectively) differ from the EDX data (La/Mn ≈ 0.81). This difference may be attributed to the presence of a Mn-rich phase in all the samples (amorphous phase or manganese oxide). Although the common formula used for the off-stoichiometric compound is LaMnO$_{3+\delta}$, the perovskite structure cannot accommodate the excess of oxygen
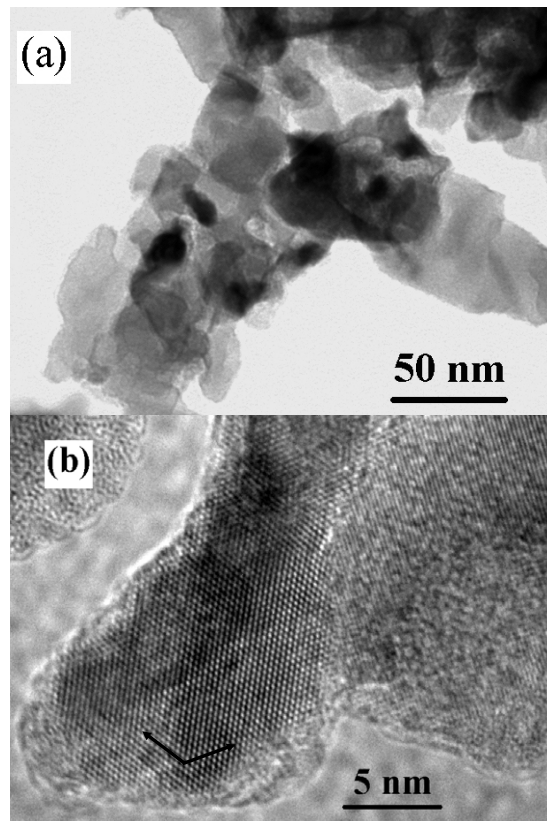
Figure 2. (a) TEM bright-field and (b) high-resolution images of sample LMO20. The $\langle 110 \rangle$ crystallographic directions are indicated by arrows.

in interstitial sites and the oxygen excess accounts for the cationic vacancies [3, 4]. In this case the chemical formula should be rewritten in the form $La_{1-x}Mn_{1-y}O_3$. Taking into account the results of Rietveld's refinement we may suggest chemical formulae $La_{0.88}MnO_3$, $La_{0.93}MnO_3$ and $La_{0.96}MnO_3$ for LMO20, LMO25 and LMO30, respectively. The thermal parameters (B) of La and Mn atoms were initially zeroed and then subsequently refined. The thermal parameter of oxygen was fixed to 2. It should be note that the accuracy of the refinement of the occupancy and thermal parameters is not so high because of the broadening of the diffraction peaks due to the nanosize of the crystallites. All the results obtained are presented in table 1. The fit of intensity versus angle for sample LMO30 is shown in figure 1(b). The results of the Rietveld's refinement mean that the more appropriate formula for our samples is $La_{1-x}MnO_{3+\delta}$, which corresponds to a concentration of Mn^{4+} equal to $3x$. In the case of the presence of vacancies in Mn sites the concentration of Mn^{4+} is $> 3x$. Then sample LMO20 with $x = 0.12$ contains Mn^{4+} with concentration higher than 36%, in agreement with the results obtained for the variation of the unit cell volume with the Mn^{4+} content [30]. Such an evaluation is in good agreement with previous experimental estimates for $La_{1-x}MnO_{3+\delta}$ nanoparticles [9].

3.2. Magnetization and ac susceptibility at $P = 0$

The ZFC and FC magnetization curves (M_{ZFC} and M_{FC}, respectively) of all LMO20, LMO25, and LMO30 samples, recorded in a low magnetic field of 10 Oe, are shown in figure 3.
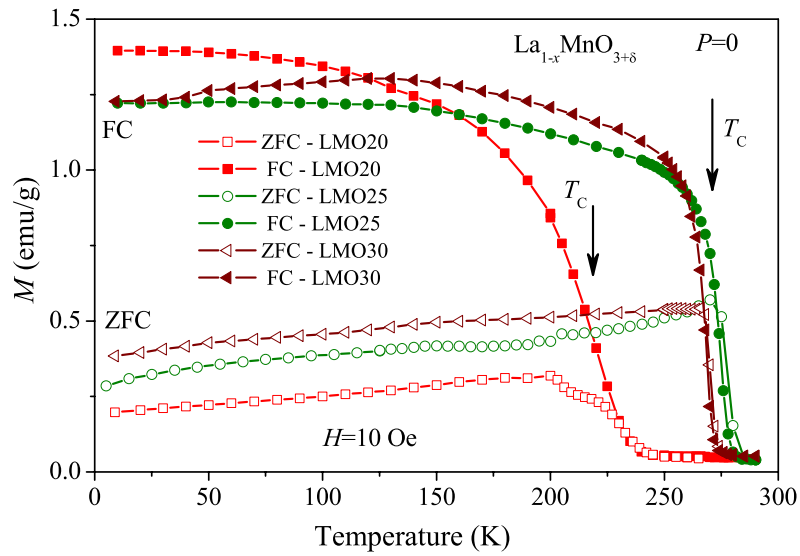
Figure 3. Temperature dependence of ZFC and FC magnetization for LMO20, LMO25, and LMO30 samples, recorded in $H = 10$ Oe.

Table 1. Results of the Rietveld refinement: lattice parameters, volume of unit cell, occupancy of La position, Debye–Waller factors (B), x_O for oxygen site position (x, 0, $\frac{1}{4}$), Mn–O–Mn angle, agreement factors (R) and transition temperature for $La_{1-x}MnO_{3+\delta}$ samples with average particles size of 20, 25, and 30 nm.

	Sample		
	LMO20	LMO25	LMO30
Lattice parameters			
a (Å)	5.508(1)	5.504(1)	5.510(1)
c (Å)	13.363(1)	13.365(1)	13.357(1)
Unit cell volume (Å^3)	58.52	58.44	58.53
Occupancy La	0.88(6)	0.93(6)	0.96(6)
B_{La} (Å^2)	0.85(10)	0.78(8)	0.70(10)
B_{Mn} (Å^2)	0.74(8)	0.62(8)	0.55(7)
x_O	0.458(6)	0.461(6)	0.459(6)
Mn–O–Mn angle (deg)	166.4	167.4	166.7
R_{wp}	13.6	11.1	9.1
R_{Bragg}	5.84	3.94	3.03
Transition temperature (K)	$\sim 220 \pm 2$	$\sim 272 \pm 2$	$\sim 268 \pm 2$

The Curie temperature of the Mn spin sublattice, T_C, was determined as the minimum in the derivative of the magnetization curves $dM_{FC}(T)/dT$. The following features are also noticeable: (i) all compounds exhibit a great difference between M_{FC} and M_{ZFC} curves; (ii) the LMO20 sample has broad magnetic transition with the lowest $T_C \approx 220 \pm 2$ K; (iii) the other samples present a sharp magnetic transition. Unexpectedly, the transition temperature of the LMO25 sample ($T_C \approx 272 \pm 2$ K) is slightly higher than that of the LMO30 sample ($T_C \approx 268 \pm 2$ K).
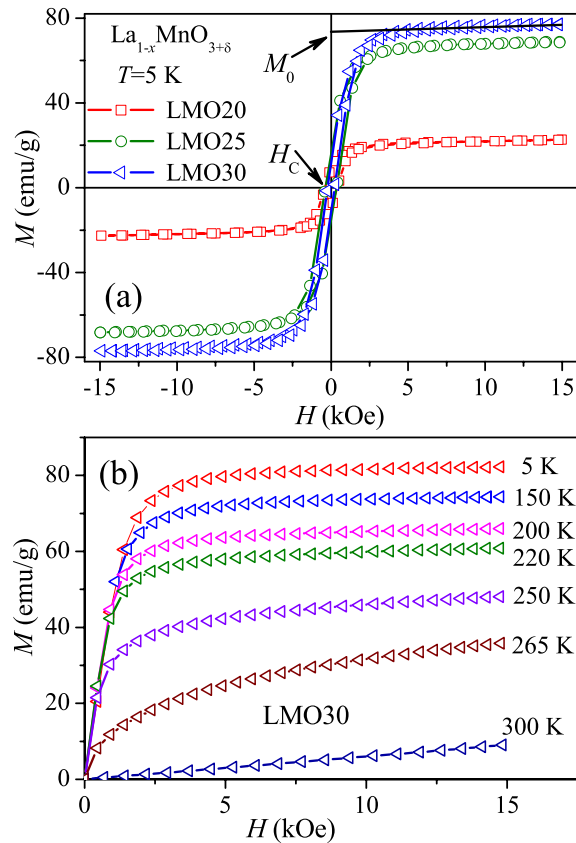
Figure 4. (a) Magnetization curves M versus H for LMO20, LMO25, and LMO30 samples at $T = 5$ K; (b) field dependence of magnetization of the LMO30 sample at various temperatures after zero-field cooling.

Figure 4(a) shows the magnetization versus magnetic field of all nanoparticle samples recorded at 5 K following zero-field cooling. As seen in figure 4(a), the spontaneous magnetization M_0, obtained by a linear extrapolation of the high-field magnetization to $H = 0$ ($M_0 \approx 20.7$, 66.1, and 74.4 emu g^{-1} for LMO20, LMO25, and LMO30, respectively), increases with increasing nanoparticle size. On the other hand, the coercive field, H_C, decreases for larger nanoparticle size ($H_C \approx 390$ Oe, 350 Oe, and 230 Oe for LMO20, LMO25, and LMO30, respectively); see figure 4(a). Figure 4(b) shows the magnetization curves $M(H)$ of sample LMO30 at various temperatures. The $M(H)$ data have been used for further analysis of the reduced magnetization $m = M(T)/M(T = 0)$, presented later in the discussion. It is seen from figure 4(b) that the magnetization of the LMO30 sample at $T = 5$ K is almost saturated in magnetic fields $H > 5$ kOe.

The temperature dependence of both the real and imaginary components of the ac susceptibility for samples LMO20 and LMO30 was measured at several frequencies ranging from 100 Hz to 10 kHz. The data for samples LMO20 (figure 5) and LMO30 (figure 6) were taken as described below. A probing ac magnetic field of 1.0 Oe amplitude was applied to measure the susceptibility as the temperature was slowly decreased in short steps from 300 to 5 K. The real part, χ', of the ac susceptibility of sample LMO20 (see figure 5(a)) exhibits a
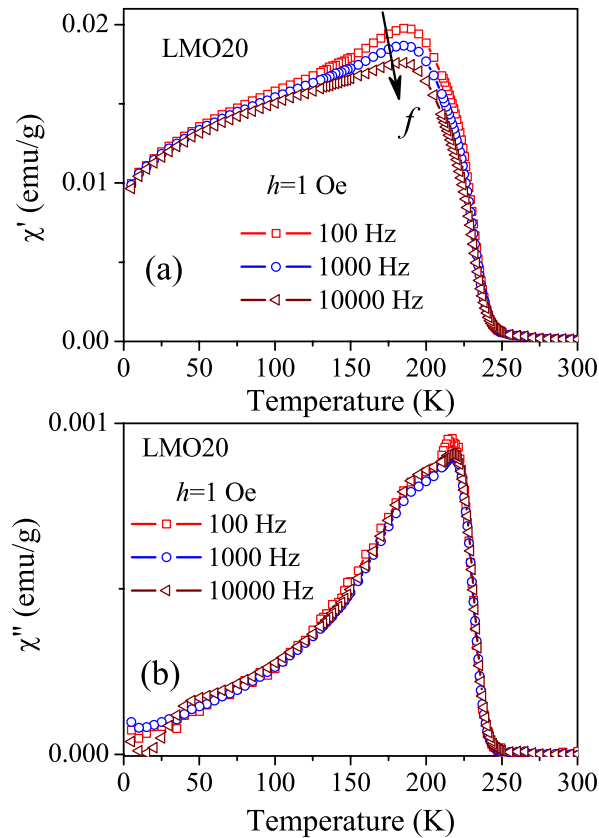
Figure 5. Temperature dependence of real (a) and imaginary (b) parts of ac susceptibility of sample LMO20 at various frequencies. The probing field has an amplitude of 1.0 Oe.

wide magnetic transition and significant dependence on frequency in a wide temperature range below $T \sim 230$ K. We note that all curves of χ' of the LMO20 sample have a bump at some temperature; as the frequency increases, the value of χ' decreases. The temperature of the bump of the in-phase component χ' ($T_p \approx 188$ K) and the corresponding inflection points of the out-of-phase χ'' component are practically the same for all frequencies. Such a behaviour is rather puzzling, because for both interacting and non-interacting nanoparticles [27, 31], as well as for spin-glasses [32], the temperature of the peak of χ' increases with increasing frequency. The out-of-phase component is almost frequency independent at all temperatures; see figure 5(b). It exhibits a peak at 217 K, then gradually decreases with decreasing temperature, exhibiting a smooth shoulder below $T \sim 188$ K. It is worth noting that the onset of dissipation, as reflected by the out-of-phase component χ'', is abrupt and indicates a spin-glass-like behaviour rather than that characteristic for both interacting and non-interacting nanoparticles [18, 19]. In a distinct contrast with the behaviour of sample LMO20, the ac susceptibility of sample LMO30 resembles a characteristic behaviour of a conventional ferromagnet. Both the in-phase component χ' and the corresponding out-of-phase χ'' exhibit an abrupt sharp peak in the vicinity of $T_C \approx 268$ K. A very weak frequency dependence of the in-phase component χ' is seen only at temperatures below T_C, possibly due to a manifestation of critical fluctuation in a system approaching a second-order paramagnetic to ferromagnetic transition.
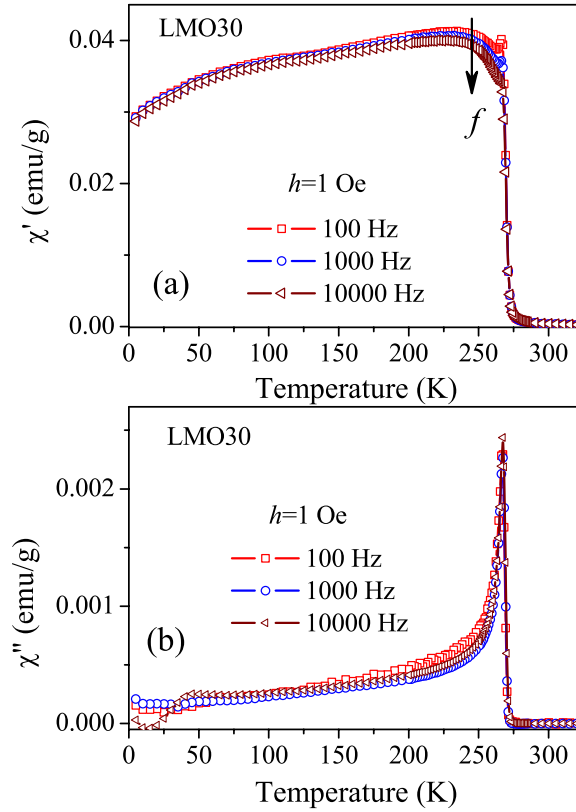
Figure 6. Temperature dependence of real (a) and imaginary (b) parts of ac susceptibility of sample LMO30 at various frequencies. The probing field has an amplitude of 1.0 Oe.

3.3. Effect of hydrostatic pressure on the magnetization

Figure 7(a) presents curves of M_{ZFC} and M_{FC} observed for the LMO20 sample at various pressures. Figure 7(b) shows the variation of M with H under pressure. An application of pressure leads to the following results: (i) the Curie temperature increases with a rate $dT_C/dP \approx 1.9$ K kbar^{-1}, see the inset to figure 7(a); (ii) M versus H curves taken at $T = 5$ K show a significant rise of spontaneous magnetization (from $M_0 \approx 20.7$ emu g^{-1} to $M_0 \approx 27$ emu g^{-1} under pressure of 12 kbar), corresponding to the increase of FM phase volume under pressure. After releasing the pressure, T_C returns to its previous value as before the application of pressure; compare the FC curves recorded at $P = 0$ before and after an application of pressure, figure 7(a). Nevertheless, the M versus H curve recorded at $P = 0$ after releasing the pressure still remains unsaturated, even in magnetic field as high as 90 kOe; see figure 7(c).

Figure 8(a) presents curves of M_{ZFC} and M_{FC} for sample LMO30 at various pressures recorded in a magnetic field of 100 Oe and 1 kOe. Similarly to the case of sample LMO25 (not shown), the Curie temperature increases by $dT_C/dP \approx 1.4$ K kbar^{-1}. After releasing the pressure, T_C returns to its previous value. The dependence of M on H at low temperatures is practically independent of pressure; see figure 8(b).

Analysing our results, we have found some bizarre magnetic and structural properties for LMO25 nanoparticles. As anticipated, we evaluated that the specific surface decreases and the
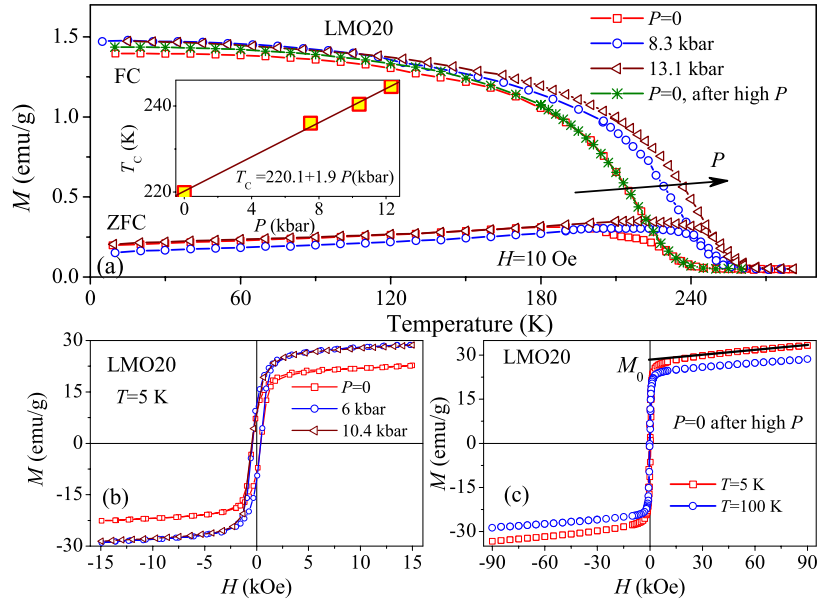
Figure 7. (a) Temperature dependence of zero-field-cooled M_{ZFC} and field-cooled M_{FC} magnetization of sample LMO20 at various pressures; (b) field dependence of magnetization of sample LMO20 at $T = 5$ K under various pressures; (c) field dependence of magnetization of sample LMO20 at $T = 5$ and 100 K under $P = 0$ after application of pressure.

spontaneous magnetization (corresponding to the volume of the FM phase, see figure 4(a)) increases monotonically upon increasing the annealing temperature. On the other hand, structural parameters such as the c lattice parameter, the volume of the unit cell, and the Mn–O–Mn angle, do not follow a monotonic variation with particle size (table 1). It is worth noting that samples LMO25 and LMO30, with comparable FM volume fraction, exhibit practically the same pressure coefficient of the Curie temperature ($dT_C/dP \approx 1.4$ K kbar^{-1}). Nevertheless, a non-regular behaviour of LMO25 regarding T_C was observed. Namely, T_C of this sample is somewhat higher than that of LMO30 (see figure 3). Therefore more detailed magnetic measurements were carried out for samples LMO20 and LMO30, which differ significantly in relative volume of the FM phase and T_C, while some supplementary results of magnetic measurements were obtained for sample LMO25.

3.4. Memory effect

An experimental observation of the memory effects in interacting permalloy $Ni_{81}Fe_{19}$ nanoparticles (average size $\sim$ 6 nm, blocking temperature $T_B = 78$ K) was reported by Sun *et al* [15] in the step-like behaviour of the temperature dependence of the magnetization. Similar experiments were carried out with superparamagnetic, non-interacting γ-Fe_2O_3 nanoparticles (average size $\sim$ 4 nm, blocking temperature $T_B = 38$ K) [16], nearly non-interacting Co nanoparticles (average size $\sim$ 5 nm, blocking temperature $T_B = 35$ K) [17], non-interacting ferritine nanoparticles (8 nm, blocking temperature $T_B = 13$ K), and a dense Fe_3N nanoparticle system [19]. It is well known [15–17, 19], that variation of an applied magnetic field may induce a sharp change in the magnetization of a particle system below its blocking temperature. Therefore, all the aforementioned dc memory experiments were carried with intermittent stops at temperatures $T < T_B$. Although sample LMO20 exhibits a clear
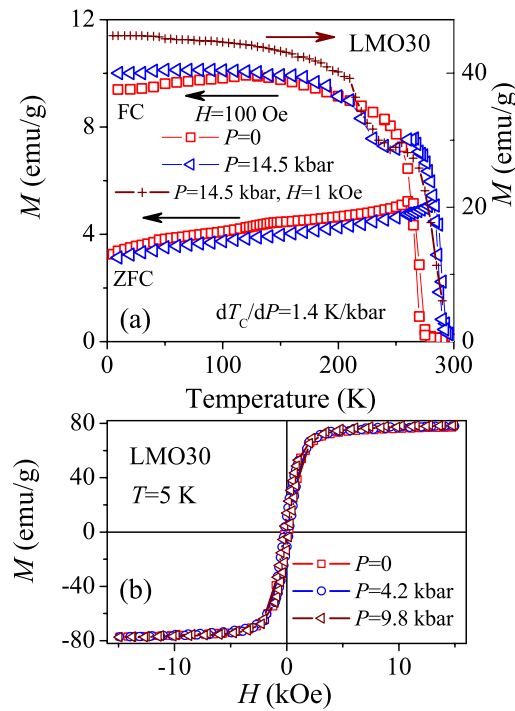
Figure 8. (a) Temperature dependence of zero-field-cooled M_{ZFC} and field-cooled M_{FC} magnetization of sample LMO30 at various pressures recorded in a magnetic field of 100 Oe and 1 kOe. (b) Field dependence of magnetization of sample LMO30 at $T = 5$ K under various pressures.

PFT at $T_C \approx 220$ K, the ZFC curve peaks at $T_{max} \approx 200$ K (figure 3), resembling hazily superparamagnetic blocking temperature of nanoparticles. We have investigated the dynamics of the FC magnetization of the LMO20 sample following the approach used by Sun *et al* [15]. The sample was initially cooled in $H = 50$ Oe from room temperature down to 5 K at a constant cooling rate of 2 K min^{-1}, then the magnetization was measured during warming; see the reference curve in figure 9. The sample was cooled again at the same rate and the magnetization was recorded during cooling, but this time with temporary stops at $T = 150, 100$ and 50 K for identical waiting times of 10^4 s. The magnetic field was turned off at the beginning of the stops and then turned on again at the end of the waiting time. The magnetization relaxed during the temporary stops and the $M(T)$ curve recorded at such a protocol has a step-like form (open squares in figure 9). After reaching the temperature of 5 K, the sample was warmed continuously at the same rate in $H = 50$ Oe, and the magnetization was recorded again (crosses in figure 9). The comparison of curves recorded with the temporary stops and the latter one shows that the system has some kind of memory of its thermal history as the curve on warming follows to some extent the step-like changes at the very same temperatures at which the system was intermittently stopped during cooling.

4. Discussion

In the following we will discuss the experimental observations in detail. A very small variation in the lattice constants was found for all $La_{1-x}MnO_{3+\delta}$ nanoparticles, having rhombohedral
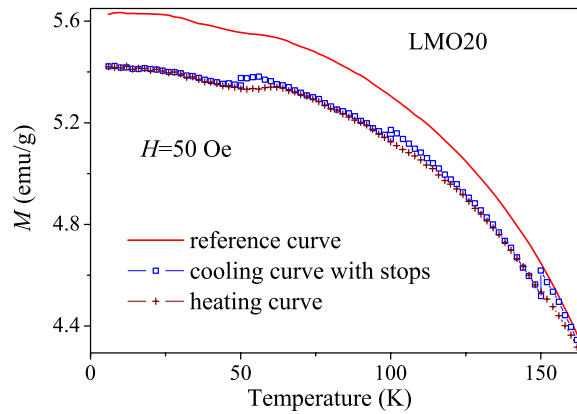
Figure 9. Memory effect in the dc magnetization of LMO20 nanoparticles. The solid line shows data recorded at a constant rate of 2 K min^{-1} after field cooling in a magnetic field of $H = 50$ Oe. The open squares show points measured during cooling in 50 Oe at the same rate with temporary stops of cooling for 10^4 s at 50, 100, and 150 K. The field was cut off during each stop. The crosses denote points measured on continuous heating with the same rate after the cooling procedure.

structure. The parent stoichiometric compound LaMnO$_3$ is an A-type antiferromagnetic insulator, in its ground state having an AFM Néel temperature $T_N \approx 140$ K [33] and an orthorhombic perovskite structure with space group P_{nma} at room temperature. Lanthanum manganites demonstrate a wide range of off-stoichiometric oxidation on the lanthanum sites as well as on the manganese sites (for self-doping). Though the common formula used for off-stoichiometric lanthanum manganites is LaMnO$_{3+\delta}$, the perovskite structure cannot accommodate the excess of oxygen in interstitial sites and the oxygen excess accounts for cationic vacancies [4, 30, 34]. The evolution of the crystal structure and magnetic order with progressive off-stoichiometry was a subject of numerous publications [4, 30, 34]. As pointed out by Topfer and Goodenough [4], orthorhombic samples with small content of cation vacancies may contain superparamagnetic clusters distributed in the AFM matrix and may exhibit a spin-glass behaviour below T_N. In the rhombohedral phase (at $\delta > 0.06$), the cooperative Jahn–Teller distortions are suppressed and the conduction electrons cause the DE interaction, which competes with antiferromagnetic superexchange, and the matrix becomes ferromagnetic.

Using the determined values of spontaneous magnetization, associated with the FM phase, we have calculated the relative volume of the FM phase in our samples, taking into account the presence of Mn$_3$O$_4$ phase (of about 4% in LMO25 and about 9% in LMO30) and the variation of the magnetic moment with its content. The contribution of Mn$_3$O$_4$ phase to $M(H)$ at 5 K was accounted for using the results of previous studies of the bulk [35] and nanoparticles [36] of Mn$_3$O$_4$. A linear reduction of the number of Bohr magnetons per Mn ion with increasing self-doping was also taken into account [4]. The calculated values obtained for the relative FM phase are 24%, 76% and 93.3% for LMO20, LMO25 and LMO30 samples, respectively. It should be noted that the saturated magnetization increases monotonically with increasing sintering temperature and particle size. This observation is consistent with the results of previous studies of the size effect in the optimally hole-doped La$_{1-x}$Ca$_x$MnO$_3$ [7] and La$_{1-x}$Sr$_x$MnO$_3$ [12, 13] with $x \sim 0.3$. It was found recently that the saturated magnetization of La$_{2/3}$Ca$_{1/3}$MnO$_3$ nanoparticles reduces linearly with the surface/volume ratio d ($d \propto$ inverse grain size) [7]. This behaviour was discussed in the frame

of a model based on an ideal inner core and an outer shell of a thickness t for which the oxygen non-stoichiometry, vacancies and stress are taken into account. In such a model, the saturated magnetization diminishes for smaller particles since the outer dead layer thickens as the particle size decreases. The outer layer inherently involves the following magnetization diminishing effects: (i) contamination of the grain surface, (ii) breaking of Mn–O–Mn paths at the grain surface, (iii) termination of the crystal structure at the grain surface, and (iiii) dislocation at the grain boundaries [8]. However, for the sake of simplicity it is usually suggested that the shell of the nanoparticles has a zero magnetization. We have found that the spontaneous magnetization and the volume of the FM phase in LMO nanoparticles decreases almost linearly with the surface/volume ratio d, supporting the above model. It was found that for sample LMO30 the outer magnetically dead shell has a thickness t of about 0.4 nm, whereas in sample LMO20 it reaches $\sim$3 nm. This observation is in an agreement with a well-established fact that the shell thickness increases with the decrease in grain size [5, 6, 8]. On the other hand, our estimation of the LMO30 sample shell thickness contravenes estimations of t for $La_{2/3}Ca_{1/3}MnO_3$ nanoparticles by López-Quintela *et al* [7], claiming that for $La_{2/3}Ca_{1/3}MnO_3$ nanoparticles of 60–500 nm, $t \approx 3$ nm, and remains almost unchanged for all sizes.

The ferromagnetic phase may be characterized by the volume fraction, spontaneous magnetization, magnetic interactions between Mn ions, and by the corresponding Curie temperature, T_C. The Curie temperature of the surface phase or of the part of core neighbouring to the shell may be lower than the T_C of the body phase [37]. Moreover, this contribution is more important as the particle size becomes smaller, resulting in a broadening of the PFT and reduction of T_C [5, 7, 14]. This fact is verified here for sample LMO20 (see figure 3).

In order to understand the above observations, we examined the nature of the magnetic interactions in manganites. It has been established that the DE is the main cause for ferromagnetism in various manganite systems [1, 2]. The intensity of DE ferromagnetic interactions and the corresponding value of T_C are proportional to the bandwidth of the conduction e_g electrons, given by [1, 2]

$$W \approx \nu^2 \cos(\phi) \cos(\theta_{ij}/2), \tag{1}$$

where ν is the covalent mixing parameter, ϕ is the bond-bending angle ($\phi = (180° - \Theta)$, Θ is Mn–O–Mn bond angle), and θ_{ij} is the angle between the two spin directions of the neighbouring manganese ions. According to equation (1) and figure 3, the bond angle Mn–O–Mn of the LMO25 and LMO30 samples should be somewhat larger than that of the LMO20 sample; see table 1. The greater Mn–O–Mn bond angle in the LMO25 sample in comparison with that of the LMO30 sample may be attributed to the effect of lattice strain, which increases with decreasing particle size [10]. Certainly, the effect of lattice strain on the increase of T_C should be the largest in the smallest-nanoparticle LMO20 sample, but in this sample the effect of the lattice strain is possibly masked by the overwhelming opposite effect of spin disorder at the surface, discussed before. One should keep in mind that the bandwidth W in the perovskite structure can be calculated for σ-bonding electrons according to the formula [38]

$$W \approx \cos(\Theta)/d_{Mn-O}^{3.5}. \tag{2}$$

Using the values of bond lengths d_{Mn-O} (1.9545, 1.9512, and 1.953 Å for samples LMO20, LMO25, and LMO30, respectively) and of bond angles (see table 1), we obtained the values of $W = 0.09323$, 0.09412 and 0.09348 (arbitrary unit) for samples LMO20, LMO25, and LMO30, respectively. Although the bandwidth for LMO25 is slightly larger than that for LMO30, a minute difference between calculated values is insufficient to validate the variation of T_C within the samples under consideration. Additional factors, such as the effects of strains and the surface, should be taken into account.

14

It is well known that the magnetic properties of manganites are very sensitive to the nominal ratio of Mn^{3+} and Mn^{4+} species. As already pointed out, the estimation for the LMO20 sample gives a value of $\sim 36\%$ of Mn^{4+}. Nevertheless, additional factors, which vary with increasing particle size and may significantly affect the magnetic state of the samples, should be taken into account. The results of [30] for polycrystalline self-doped $LaMnO_{3+\delta}$ samples have shown that the Mn^{4+} content decreases with increasing annealing temperature, resulting in an increasing level of non-stoichiometry for samples annealed at lower temperature. Moreover, sample LMO20 contains a noticeable amount of amorphous phase, while both LMO25 and LMO30 samples, annealed at higher temperatures, are better crystallized. Moreover, the presence of the parasitic Mn_3O_4 phase (about 4% in LMO25 and about 9% in LMO30) should also reduce the oxygen content, affecting the magnetic properties such as T_C and saturation magnetization. All the above factors may result in observed maximum of T_C for sample LMO25.

One of the open issues in studies of manganites is the character of the magnetic transition. This dilemma also concerns our discussion on LMO nanoparticles: is the PFT of a second order, reflecting the intensity of the magnetic interactions (T_C), or it is of a different nature?

Recently, the character of the magnetic transition at T_C in manganites has been examined in a number of papers [39–45]. Despite the efforts made, the nature of magnetic transition in some cases is controversial. For the $La_{1-x}Ca_xMnO_3$ system it was shown that the character of the PFT at T_C depends on the level of Ca doping. In particular, Rivadulla *et al* [45] have shown recently that the PFT in $La_{1-x}Ca_xMnO_3$ is of a first order only in the compositional range $0.275 < x < 0.43$, whereas close to the localized-to-itinerant electronic transition, at $x \approx 0.2$ and $x \approx 0.5$, the system does not undergo a true magnetic transition due to an occurrence of a random field which breaks up the magnetic homogeneity of the system. In the case of magnetic nanoparticles, the nature of the PFT may depend, in addition to that, on the size of the particles. The magnetic measurements [7, 11] have shown that relatively large $La_{2/3}Ca_{1/3}MnO_3$ nanoparticles with size 95–500 nm exhibit a first-order PFT, whereas a second-order magnetic phase transition has been realized in the smallest particles of 60 nm. We examined the nature of the PFT in $La_{1-x}MnO_{3+\delta}$ nanoparticles within the classical model of Bean and Rodbell (BR) [46] in which the dependence of exchange energy on the interatomic distances is taking into account. The main ideas and results of the BR model were used to distinguish the nature of magnetic transition in manganites [39, 42–44]. In particular, Novak *et al* [39] have extended the BR model for the case the DE interaction in manganites, containing Mn ions of different valence. They have shown that the criterion suggested by the BR model to distinguish a first-order and a second-order transition, based on the temperature dependence of the reduced magnetization, is also valid in the case of manganites with DE ferromagnetic interaction. The experimental dependence of reduced magnetization is compared with curves calculated within the BR model for different coupling parameters, n, which depends on the number of parameters of the system such as spin moment, compressibility, and Curie temperature [39, 46]. For $n < 1$, the magnetic transition is of a second order, whereas for $n > 1$ it is of a first order. Figure 10(a) shows the temperature dependence of the reduced magnetization m of samples LMO20 and LMO30, determined from the measurements at ambient pressure, as well as the calculated BR curves for spin $S = 2$. It is clearly seen (see figure 10(a)) that the character of the $m(T)$ dependence for the LMO30 sample is rather different than that of the LMO20 sample. One may consider the PFT of the LMO30 sample to be second order ($n \sim 0.5$), whereas for LMO20 the experimental points lie even below the curve for $n = 0$. The reason for this behaviour may originate from the different magnetic states of the core and shell of each sample. The LMO30 sample exhibits a relatively sharp magnetic transition, indicating the presence of a uniform FM phase with a clear Curie transition temperature and a very small effect of the outer layer. On the other hand,
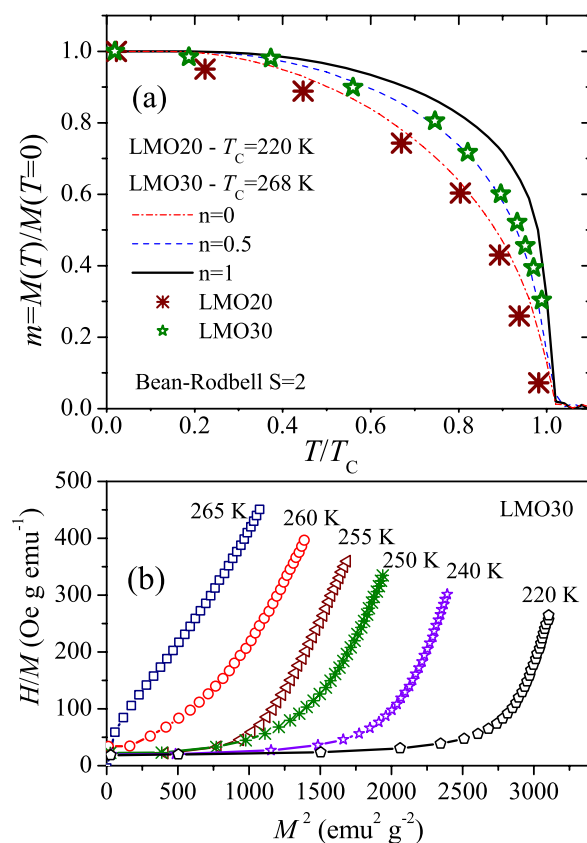
Figure 10. (a) The temperature dependence of the reduced magnetization $m = M(T)/M(T = 0)$ for samples LMO20 and LMO30. The experimental results are compared with prediction of the model of Bean and Rodbell; (b) H/M versus M^2 plot for isotherms of magnetization presented for sample LMO30 in figure 4(b). The slope is always positive, denoting the second-order character of the phase transition.

in the case of the LMO20 sample the effect of the outer layer and the structure inhomogeneity are more significant, and may result in a smearing out of the transition, resulting in a decrease of T_C. Other approaches are often used for analysis of the PFT, namely the H/M versus M^2 plot is analysed. Then, a positive slope is an indication of a second-order phase transition while a negative slope is an indication of a first-order one. This criterion, proposed by Banerjee [47], was already successfully applied to determine the change in the order of the phase transition in various manganite bulk [39] and nanoparticle [40] systems. The slope of the curves presented in figure 10(b) for the LMO30 sample is always positive, supporting the conclusion of the second-order character of the PFT in the LMO30 sample. It should be mentioned that the applicability of all these trials to inhomogeneous and strained nanoparticle systems may be questionable. It appears from examination by a Bean and Rodbell [46] like analysis and the Banerjee [47] criterion that for relatively large (30 nm) $La_{1-x}MnO_{3+\delta}$ nanoparticles the magnetic transition is of second order. In contrast, as the size of the particles decreases (20 nm case) the nature of the magnetic transition remains questionable, possibly due to the variation of T_C in the volume of the particles and the corresponding smearing out of the transition.

Let us return back to the issue of the pressure–T_C relation in LMO nanoparticles. Numerous experimental studies [21–23, 48–50] of the pressure effect on various hole-doped

manganites revealed an increase of T_C under an applied pressure. According to the DE model the pressure coefficient of the Curie temperature T_C, due to the variation of steric factors, can be evaluated according to the relation [48]

$$d \ln T_C/dP = -3.5 \, \kappa \, (d_{Mn-O}) - 2 \tan(\Theta)\Theta \, \kappa \, (\Theta), \tag{3}$$

where $\kappa(d_{Mn-O})$ and $\kappa(\Theta)$ are the bond length and bond angle compressibility, respectively. Using equation (3) and the known values for bond and angle compressibility of other manganite systems [23], one obtains $d \ln T_C/dP \sim 0.001$ kbar^{-1}. In our experiments we observed much larger values for $d \ln T_C/dP$: 0.0082, 0.0050, and 0.0051 kbar^{-1} for LMO20, LMO25 and LMO30, respectively, indicating that additional contributions should be taken into account. In particular, it was suggested that lattice-polaronic effects associated with strong electron–phonon (el–ph) coupling of Jahn–Teller type should be taken into account as well [50–52]. Indeed, a significant reduction in the Jahn–Teller effect under applied pressure was observed [50], in agreement with our observations of a pronounced dependence of T_C on pressure. One may also refer to calculations based on the experimental pressure dependence of the Jahn–Teller phonon frequency for $La_{0.75}Ca_{0.25}MnO_3$, showing that even a modest pressure may induce a considerable reduction of el–ph coupling ($\sim$7% at 10 kbar) [50].

Magnetic interactions may also be responsible for the T_C versus applied pressure dependence. It was found that hole-doped manganites at $x > x_C$ (where x_C denotes the percolation threshold) exhibit an FM metallic ground state and dominant DE interactions and, in general, a pronounced pressure coefficient $dT_C/dP \approx (1.5–2)$ K kbar^{-1}. On the other hand, hole-doped manganites at $x < x_C$ are usually characterized by weak sensitivity to applied pressure ($dT_C/dP \approx (0.2–0.3)$ K kbar^{-1}) [21, 22, 48–50]. The above observations are attributed to the different nature of FM interactions [44] for $x > x_C$ with respect to those for $x < x_C$. In the case of $x > x_C$, DE dominates the magnetic and transport properties of manganites, whereas at $x < x_C$ the DE is partly replaced by other types of FM interaction, e.g., superexchange. The pressure coefficient of T_C observed for LMO manganite nanoparticles $\sim$1.5 K kbar^{-1} (see figures 7(a) and 8(a)) is comparable with that observed for hole-doped manganites with doping level $x > x_C$. Therefore, one can conclude that the predominant FM interaction in the FM core of LMO nanoparticles is the DE interaction, which is highly sensitive to applied pressure, especially in the case of the Jahn–Teller distortions and of el–ph coupling, which are significantly suppressed under pressure. It was revealed previously that the pressure coefficient $d \ln T_C/dP$ of various hole-doped manganites decreases almost linearly with increasing Curie temperature [48]. A smaller value of the pressure coefficient $d \ln T_C/dP$ for LMO25 and LMO30 samples, in comparison with that for the LMO20 sample, indicates that the results for LMO nanoparticles are in qualitative agreement with the observed results for hole-doped bulk manganites. On the other hand, additional factors may also affect the pressure coefficient of T_C. The evaluation of the total amount of Mn^{4+} from the formula $La_{0.88}MnO_3$ gives a value of $\sim$36% in an agreement with results of [30], showing that the lower temperature of calcinations for the LMO20 sample should result in higher hole concentration. The presence of amorphous phase in the LMO20 sample and parasitic Mn_3O_4 phase in the LMO25 and LMO30 samples also complicates the situation. Moreover, the shell with a higher concentration of crystalline defects is thicker in the LMO20 sample than that in the LMO30 sample, probably leading to an enhanced compressibility of the LMO20 sample and higher dT_C/dP.

Let us discuss the memory effects observed in LMO20 nanoparticles (figure 9) following the protocol proposed by Sun *et al* [15]. They have suggested that the step-like behaviour of dc magnetization observed during reheating is caused by memory effects, inherent to the spin-glass-like phase and a hierarchical organization of metastable states resulting from significant

17

interparticle interactions. Further studies have shown that similar memory effects can be reproduced in a non-interacting nanoparticle assembly in which the distribution of relaxation times originates from the particle size distribution [16–19]. One cannot therefore exclude irregularities in the shape and variations in size of small particles (figure 2), which may be responsible for the memory effects. Sasaki *et al* [19] have analytically studied the dynamics of non-interacting nanoparticle systems such as ferritin (a superparamagnet) and dense Fe_3N nanoparticles (superspin glass). They concluded that ageing and memory effects are not a decisive proof for the existence of spin-glass dynamics, and from the memory experiment solely (such as presented in figure 9) one cannot drawn any conclusion about whether a nanoparticle system is a non-interacting superparamagnet or an interacting spin glass [19]. It appears that additional measurements such as ZFC magnetization measurements with a stop during cooling or study of nonlinear susceptibility with an appropriate protocol are required to confirm the spin-glass dynamics [53, 54]. On the other hand, Sasaki *et al* [19] pointed out that the FC magnetization of a superparamagnet always increases with decreasing temperature, whereas it is nearly constant at $T \leqslant T_C$ for a superspin glass. Quite recently, Sankar and Joy [55] observed ageing and memory effects in bulk non-stoichiometric $LaMnO_{3.13}$ in time-dependent dc magnetic measurements with various cooling protocols employed. They concluded that the results observed can be best described by the superspin glass model of an interacting magnetic nanoparticle system [55]. On the other hand, we notice that in distinct contrast with magnetization of sample LMO20 (figures 3 and 7), the magnetization of $LaMnO_{3.13}$ [55] resembles the ZFC and FC magnetization for interacting nanoparticles with the average blocking temperature $T_B = 41$ K and thermomagnetic irreversibility between ZFC and FC magnetization below T_B. It has been shown [19, 20] that in the case of the nanoparticle assembly the temperature independence of the FC magnetization for a superspin glass cannot be explained by the individual particle model and is a clear indication of progressive freezing of particle moments. Based on the above qualitative arguments and taking into account the gap between ZFC and FC magnetizations, the flatness of FC magnetization at $T < 60$ K (figure 3), the frequency dependence of the ac susceptibility in a wide temperature range (figure 5(a)) and some kind of memory effect (figure 9), we may only suggest that the LMO20 nanoparticle system resembles a superspin glass. Certainly, these are only tentative indications of the nature of the memory effect in the LMO20 sample and additional more appropriate studies (see for example [18, 19, 54]) of the dynamics of the LMO20 sample are necessarily needed for a better understanding of the memory effects and the spin dynamics.

5. Conclusions

Measurements of zero-field-cooled magnetization and sequential measurements upon cooling under the same field at ambient pressure and at an applied quasi-hydrostatic pressure were carried out on nanocrystalline manganites $La_{1-x}MnO_{3+\delta}$ with particle size of 20, 25, and 30 nm, prepared by the citrate method. It appears from the results of the magnetization measurements that all nanoparticles samples exhibit a paramagnetic to ferromagnetic transition at temperatures $T_C \approx 220 \pm 2$ K, 272 ± 2 K, 268 ± 2 K for $La_{1-x}MnO_{3+\delta}$ nanoparticles with average size of 20, 25, and 30 nm, respectively. Their relative FM volume increases with increasing particle size and approaches a value of about 93% for nanoparticles with average size of 30 nm. The real part of the ac susceptibility of 20 nm particles exhibits a bump at $T \sim 188$ K and considerable frequency dependence in wide temperature range below T_C, whereas for 30 nm particles, only a weak frequency dependence is observed in the vicinity of T_C. Using the criteria given by Banerjee and Bean and Rodbell, we have found that the magnetic transition for 30 nm nanoparticles is of a second order, while for 20 nm nanoparticles the nature of the magnetic transition cannot be determined from our magnetization measurements.

It was found that an applied pressure enhances the Curie temperature of all $La_{1-x}MnO_{3+\delta}$ nanoparticles with a pressure coefficient $dT_C/dP \approx 1.9$ K kbar^{-1} for 20 nm nanoparticles and $dT_C/dP \approx 1.4$ K kbar^{-1} for both 25 and 30 nm nanoparticle samples. The pressure coefficients $d \ln T_C/dP$ observed for $La_{1-x}MnO_{3+\delta}$ nanoparticles are comparable with that obtained for bulk hole-doped manganites and are found to be in accordance with the double-exchange-driven ferromagnetism.

Some kind of dc magnetization memory effect was observed in the 20 nm nanoparticles in a wide temperature range below T_C. Similar phenomena were previously observed [15–17] in small single-domain magnetic particles below the blocking temperature. In order to understand better the nature of the memory effect observed here in 20 nm nanoparticles, further detailed investigations are still needed.

Acknowledgments

References

[1] Dagotto E 2003 *Nanoscale Phase Separation and Colossal Magnetoresistance* (*Springer Series in Solid State Physics* vol 136) (Berlin: Springer)
[2] Goodenough J B, 2003 Rare earth-manganese perovskites *Handbook on the Physics and Chemistry of Rare Earth* vol 33, ed K A Gschneidner Jr, J-C G Bunzli and V Pecharsky (Amsterdam: Elsevier Science)
[3] van Roosmalen J A M, Cordfunke E H P, Helmholdt R B and Zandbergen H W 1994 *J. Solid State Chem.* **110** 100
   van Roosmalen J A M and Cordfunke E H P 1994 *J. Solid State Chem.* **110** 106
[4] Topfer J and Goodenough J B 1997 *J. Solid State Chem.* **130** 117
   Topfer J and Goodenough J B 1997 *Chem. Mater.* **9** 1467
[5] Zhang N, Ding W, Zhong W, Xing D and Du Y 1997 *Phys. Rev.* B **56** 8138
[6] Zhu T, Shen B G, Sun J R, Zhao H W and Zhan W S 2001 *Appl. Phys. Lett.* **78** 3863
[7] López-Quintela M A, Hueso L E, Rivas J and Rivadulla F 2003 *Nanotechnology* **14** 212
[8] Dey P and Nath T K 2006 *Phys. Rev.* B **73** 214425
[9] Dezanneau G, Audier M, Vincent H, Meneghini C and Djurado E 2004 *Phys. Rev.* B **69** 014412
   Dezanneau G, Sin A, Roussel H, Audier M and Vincent H 2003 *J. Solid State Chem.* **173** 216
   Dezanneau G, Sin A, Roussel H, Audier M and Vincent H 2002 *Solid State Commun.* **121** 133
[10] Das N, Mondal P and Bhattacharya D 2006 *Phys. Rev.* B **74** 014410
[11] Rivas J, Hueso L E, Fondado A, Rivadulla F and López-Quintela M A 2000 *J. Magn. Magn. Mater.* **221** 57
   Hueso L E, Sande P, Miguéns D R, Rivas J, Rivadulla F and López-Quintela M A 2002 *J. Appl. Phys.* **91** 9943
[12] Balcells L1, Fontcuberta J, Martinez B and Obradors X 1998 *Phys. Rev.* B **58** R14697
[13] Gaur A and Varma G D 2006 *J. Phys.: Condens. Matter* **18** 8837
[14] Moreira M L, Sores J M, de Azevedo W M, Rodrigues A R, Machado F L A and de Araújo J H 2006 *Physica* B **384** 51
[15] Sun Y, Salamon M B, Garnier K and Averback R S 2003 *Phys. Rev. Lett.* **91** 167206
[16] Tsoi G M, Wenger L E, Senaratne U, Tackett R J, Buc E C, Naik R, Vaishnava P P and Naik V 2005 *Phys. Rev.* B **72** 014445
   Tsoi G M, Senaratne U, Tackett R J, Buc E C, Naik R, Vaishnava P P, Naik V M and Wenger L E 2005 *J. Appl. Phys.* **97** 10J507
[17] Zheng R K, Gu H, Xu B and Zhang X X 2005 *Phys. Rev.* B **72** 014416
[18] Jonsson T, Nordblad P and Svedlindh P 1998 *Phys. Rev.* B **57** 497
   Hansen M F, Jönsson T, Nordblad P and Svedlindh P 2002 *J. Phys.: Condens. Matter* **14** 4901
[19] Sasaki M, Jönsson P E, Takayama H and Nordlad P 2004 *Phys. Rev. Lett.* **93** 139701
   Sasaki M, Jönsson P E, Takayama H and Mamiya H 2005 *Phys. Rev.* B **71** 104405
[20] Bandyopadhyay M and Dattagupta S 2006 *Phys. Rev.* B **74** 214410

[21] Arnold Z, Kamenev K, Ibarra M R, Algarabel P A, Marquina C, Blasco J and Garcia J 1995 *Appl. Phys. Lett.* **67** 2875
[22] Neumeier J J, Hundley M F, Thompson J D and Heffner R H 1995 *Phys. Rev.* B **52** R7006
[23] Radaelli P G, Iannone G, Marezio M, Hwang H Y, Cheong S W, Jorgensen J D and Argyriou D N 1997 *Phys. Rev.* B **56** 8265
[24] Pinsard-Gaudart L, Rodriguez-Carvajal J, Daoud-Aladine A, Goncharenko I, Medarde M, Smith R I and Revcolevschi A 2001 *Phys. Rev.* B **64** 064426
[25] Baythoun M S G and Sale F R J 1982 *Mater. Sci.* **17** 2757
[26] Krupichka E, Reller A and Weidenkaff A 2002 *Cryst. Eng.* **5** 195
[27] Baran M, Dyakonov V, Gladczuk L, Levchenko G, Piechota S and Szymczak H 1995 *Physica* C **241** 383
[28] Thompson J D 1984 *Rev. Sci. Instrum.* **55** 231
    Eremets M I 1996 *High Pressure Experimental Methods* (Oxford: Oxford University Press)
[29] Rodrigues-Carvajal J 1990 FullProf: a program for Rietveld refinement and pattern matching analysis *Abstracts of the Satellite Mtg on Powder Diffraction of the XV Congr. of the IUCR (Toulouse, France)* p 127
[30] Maurin I, Barboux P, Lassailly Y, Boilot J-P, Villain F and Dordor P 2001 *J. Solid State Chem.* **160** 123
    Maurin I, Barboux P, Lassailly Y, Boilot J-P and Villain F 2000 *J. Magn. Magn. Mater.* **211** 139
[31] Tiwari S D and Rajeev K P 2005 *Phys. Rev.* B **72** 104433
[32] Mydosh J A 1993 *Spin Glasses* (London: Taylor and Francis)
[33] Wollan E O and Koehler W C 1955 *Phys. Rev.* **100** 545
[34] Ritter C, Ibarra M R, De Teresa J M, Algarabel P A, Marquina C, Blasco J, Garcia J, Oseroff S and Cheong S-W 1997 *Phys. Rev.* B **56** 8902
[35] Srinivasan G and Seehra M S 1983 *Phys. Rev.* B **28** 1
[36] Winkler E, Zysler R D and Fiorani D 2004 *Phys. Rev.* B **70** 174406
[37] Staduik Z M, Griesbach P, Dehe G, Gütlich P, Kohara T and Stroink G 1987 *Phys. Rev.* B **35** 6588
[38] Medarde M, Mesot J, Lacorre P, Rosenkranz S, Fisher P and Gobrecht K 1995 *Phys. Rev.* B **52** 9248
[39] Novak P, Marysko M, Savosta M M and Ulyanov A N 1999 *Phys. Rev.* B **60** 6655
[40] Mira J, Rivas J, Rivadulla F, Vazquez-Vazquez C and Lopez-Quintela M A 1999 *Phys. Rev.* B **60** 2998
    Mira J, Rivas J, Hueso L E, Rivadulla F, Lopez-Quintela M A, Senaris Rodriquez M A and Ramos C A 2001 *Phys. Rev.* B **65** 024418
[41] Adams C P, Lynn J W, Smolyaninova V N, Biswas A, Greene R L, Ratcliff W II, Cheong S W, Mukovskii Y M and Shulyatev D A 2004 *Phys. Rev.* B **70** 134414
    Li W, Kunkel H P, Zhou X Z, Williams G, Mukovskii Y and Shulyatev D 2004 *J. Phys.: Condens. Matter* **16** L109
[42] Laukhin V, Martínez B, Fontcuberta J and Mukovskii Y M 2001 *Phys. Rev.* B **63** 214417
[43] Arkhipov V E, Bebenin N G, Dyakina V P, Gaviko V S, Korolev A V, Mashkautsan V V, Neifeld E A, Zainullina R I, Mukovskii Ya M and Shulyatev D A 2000 *Phys. Rev.* B **61** 11229
[44] Reis M S, Amaral V S, Araújo J P and Oliveira I S 2003 *Phys. Rev.* B **68** 014404
[45] Rivadulla F, Rivas J and Goodenough J B 2004 *Phys. Rev.* B **70** 172410
[46] Bean C P and Rodbell D S 1962 *Phys. Rev.* **126** 104
[47] Banerjee S K 1964 *Phys. Lett.* **12** 16
[48] Laukhin V, Fontcuberta J, García-Munoz J L and Obradors X 1997 *Phys. Rev.* B **56** R10009
[49] Markovich V, Fita I, Puzniak R, Tsindlekht M I, Wisniewski A and Gorodetsky G 2002 *Phys. Rev.* B **66** 094409
    Markovich V, Rozenberg E, Shames A I, Gorodetsky G, Fita I, Suzuki K, Puzniak R, Shulyatev D A and Mukovskii Ya M 2002 *Phys. Rev.* B **65** 144402
    Markovich V, Fita I, Puzniak R, Wisniewski A, Suzuki K, Cochrane J W, Yuzhelevskii Y, Mukovskii Ya M and Gorodetsky G 2005 *Phys. Rev.* B **71** 224409
[50] Postorino P, Congeduti A, Dore P, Sacchetti A, Gorelli F, Ulivi L, Kumar A and Sarma D D 2003 *Phys. Rev. Lett.* **91** 175501
    Postorino P, Sacchetti A, Capone M and Dore P 2004 *Phys. Status Solidi* b **241** 3381
    Sacchetti A, Postorino P and Capone M 2006 *New J. Phys.* **8** 3
[51] De Teresa J M, Ibarra M R, Algarabel P A, Ritter C, Marquina C, Blasco J, Garcia J, del Moral A and Arnold Z 1997 *Nature* **386** 256
[52] Garbarino G, Acha C, Vega D, Leyva G, Polla G, Martin C, Maignan A and Raveau B 2004 *Phys. Rev.* B **70** 014414
[53] Mathieu R, Jönsson P, Nam D N H and Nordblad P 2001 *Phys. Rev.* B **63** 092401
[54] Rivadulla F, López-Quintela M A and Rivas J 2004 *Phys. Rev. Lett.* **93** 167206
[55] Sankar C R and Joy P A 2005 *Phys. Rev.* B **72** 132407